Journal of Luminescence 146 (2014) 321–324

Contents lists available at ScienceDirect

Journal of Luminescence

journal homepage: www.elsevier.com/locate/jlumin

Optical properties and energy transfers of Ce^{3+} and Mn^{2+} in $Ba_9Sc_2(SiO_4)_6$

Xia Zhang [a], Yongfu Liu [a,*], Jian Lin [a,b], Zhendong Hao [a], Yongshi Luo [a], Qingzhe Liu [c], Jiahua Zhang [a,*]

[a] State Key Laboratory of Luminescence and Applications, Changchun Institute of Optics, Fine Mechanics and Physics, Chinese Academy of Sciences, 3888 Eastern South Lake Road, Changchun 130033, China
[b] Graduate School of Chinese Academy of Sciences, Beijing 100039, China
[c] Department of Physics, Northwest University, Xi'an 710069, China

ARTICLE INFO

Article history:
Received 3 July 2013
Received in revised form
7 September 2013
Accepted 5 October 2013
Available online 12 October 2013

Keywords:
$Ba_9Sc_2(SiO_4)_6:Ce^{3+}$, Mn^{2+}
Luminescence
Energy transfer
White LED

ABSTRACT

Analysis of XRD patterns indicates that Ce^{3+} and Mn^{2+} in $Ba_9Sc_2(SiO_4)_6$ (BSS) presents preferably at the Sc^{3+} and the Ba^{2+} site, respectively. $Ba_9Sc_2(SiO_4)_6:Ce^{3+}$ (BSS:Ce^{3+}) exhibits an intense emission band peaked at 383 nm. Codoping Mn^{2+} into this material can generate a red emission band at 615 nm of Mn^{2+} through Ce^{3+}–Mn^{2+} energy transfers (ETs). To achieve the ET mechanisms, critical distance and coefficient, the dynamical processes of the ET are investigated based on Inokuti–Hirayama model. For Ce^{3+} concentration of 5 mol%, the corresponding rate constant and the critical distance are evaluated to be 8.4×10^{-37} cm^6 s^{-1} and 0.52 nm, respectively. The ET efficiency can reach 48%. The emission intensity ratio of the Mn^{2+} to the Ce^{3+} is also studied to understand color-tunable luminescence as the blue Ce^{3+} is excited by UV light. These results show the promising application of this phosphor for white LEDs.

1. Introduction

Phosphor-converted white light emitting diode (pc-WLED) is regarded as a new lighting source for the next generation. The most current pc-WLEDs employ blue InGaN LEDs combined with yellow-emitting $Y_3Al_5O_{12}:Ce^{3+}$ (YAG:Ce^{3+}) garnet phosphors [1,2]. However, since lacking in a red component, the mixed light emitted by this type has a poor color rendering index ($R_a < 80$) and a high correlated color temperature (CCT > 5000 K). One of the alternative ways to achieve white light with a suitable CCT and a high R_a is the combination of ultraviolet (UV) LEDs with the red, green and blue (RGB) multi-phased phosphors [3]. However, one of the significant drawbacks of this way is the lacking in high efficiency red phosphors.

Mn^{2+} is a kind of commonly used UV-excited red light emission ion. Depending on the crystal field of the host materials the emission spectrum of the Mn^{2+} ranges from green to deep red (500–700 nm) [4,5]. However, the biggest obstacle for the application of the Mn^{2+} used as good candidates for red phosphors is that the d–d absorption transition is difficult to be pumped. Since this transition is strongly parity forbidden, and therefore, seldom Mn^{2+} singly doped hosts can act as applicable phosphors [6]. In order to improve the emission intensity of Mn^{2+}, Ce^{3+} or Eu^{2+} is widely used as sensitizers in many Mn^{2+}-doped hosts such as $KCaY(PO_4)_2:Eu^{2+}$, Mn^{2+} [7], $SrAl_2O_4:Ce^{3+}$, Mn^{2+} [8], and $Ca_3Sc_2Si_3O_{12}:Ce^{3+}$, Mn^{2+} [9].

In 2009, a novel green-emitting phosphor of Eu^{2+} doped $Ba_9Sc_2(SiO_4)_6$ (BSS) was reported by Nakano et al., which can be used in pc-WLED [10]. In this paper, we report a strong UV-blue emission in the range of 350–450 nm by doping Ce^{3+} into the BSS host. By codoping Mn^{2+} into BSS:Ce^{3+}, furthermore, an intense Mn^{2+} red emission band at 615 nm is achieved due to the effective energy transfers (ETs) from Ce^{3+} to Mn^{2+}, which indicates that BSS:Ce^{3+}, Mn^{2+} can also be used as red phosphors for white LEDs.

2. Experimental procedure

A series of $Ba_9Sc_2(SiO_4)_6:Ce^{3+}$, Mn^{2+} samples investigated in this work were synthesized by solid state reactions. The constituent oxides or carbonates $BaCO_3$ (99.99%), Sc_2O_3 (99.99%), SiO_2 (99.99%), CeO_2 (99.99%), $MnCO_3$ (99.99%) were intimately mixed according to stoichiometric ratios. The mixtures were sintered at 1350 °C for 3 h in a 5% H_2+95% N_2 reductive atmosphere. XRD data were collected using a Bruker D8 Advance diffractometer. To clarify the preferable location of Ce^{3+} and Mn^{2+} in the BSS structure, the high resolution XRD profiles were recorded with a

* Corresponding author. Tel.: +86 431 8670 8875; fax: +86 431 8670 8875.
E-mail addresses: liuyongfu1985@126.com (Y. Liu), zhangjh@ciomp.ac.cn (J. Zhang).

0022-2313/$ - see front matter © 2013 Elsevier B.V. All rights reserved.
http://dx.doi.org/10.1016/j.jlumin.2013.10.017

step size of 0.0014° (2θ) in the range of 30–32°. To perform the phase purity of samples, XRD profiles were recorded in the range of 15–75°. Photoluminescence (PL), photoluminescence excitation (PLE) and diffuse reflectance (DR) spectra were measured using a Hitachi F-4500 Spectrometer equipped with a 150 W xenon lamp under a working voltage of 700 V. Both the excitation and emission slits were set at 2.5 nm. In fluorescence lifetime measurements, the third harmonic (355 nm) of an Nd-doped yttrium aluminum garnet pulsed laser (Spectra- Physics, GCR 130) was used as an excitation source for the Mn^{2+} lifetime measurement, and the signals were detected with a Tektronix digital oscilloscope (TDS 3052). The Ce^{3+} fluorescence lifetime was measured by FL920 Fluorescence Lifetime Spectrometer with the time resolution of 2 ns.

3. Results and discussion

3.1. Crystal characterization

$Ba_9Sc_2(SiO_4)_6$ was firstly reported to be crystallized by Wang et al. [11], which belongs to a rhombohedral system with space group of $R\bar{3}$ and lattice parameters of a=9.8716(2) Å and b=21.9376 Å. There is only one site for Sc^{3+} and Si^{4+} with coordination numbers (CNs) of 6 and 4 in BSS, respectively. However, there are three sites for Ba^{2+} ions in the structure, which are Ba(1), Ba(2), and Ba(3) with CN of 12, 9, and 10, respectively. To clarify the location of Ce^{3+} and Mn^{2+} in the BSS structure, samples with the nominal compositions of $(Ba_{9-x}Ce_x)Sc_2(SiO_4)_6$, $Ba_9(Sc_{2-x}Ce_x)(SiO_4)_6$, $(Ba_{9-y}Mn_y)Sc_2(SiO_4)_6$, and $Ba_9(Sc_{2-y}Mn_y)(SiO_4)_6$ (x=0.01, 0.05, 0.10 and y=0.05, 0.10, 0.20) were prepared. The high resolution XRD patterns of these samples were recorded and shown in Fig. 1. The XRD peaks of the series samples with nominal Ce^{3+} occupations either at the Ba^{2+} sites (Fig. 1(a)) or at the Sc^{3+} sites (Fig. 1(b)) shift to small angle regions with increasing Ce^{3+} ions. This result indicates that crystal expansions occur for Ce^{3+} presents either at the Ba^{2+} sites or at the Sc^{3+} sites. While the XRD peaks of the samples with nominal Mn^{2+} occupations at the Ba^{2+} sites (Fig. 1(c)) or at the Sc^{3+} sites (Fig. 1(d)) shift to high angle regions with increasing Mn^{2+} ions. This indicates that crystal contractions occur for Mn^{2+} presents at either at the Ba^{2+} sites or the Sc^{3+} sites.

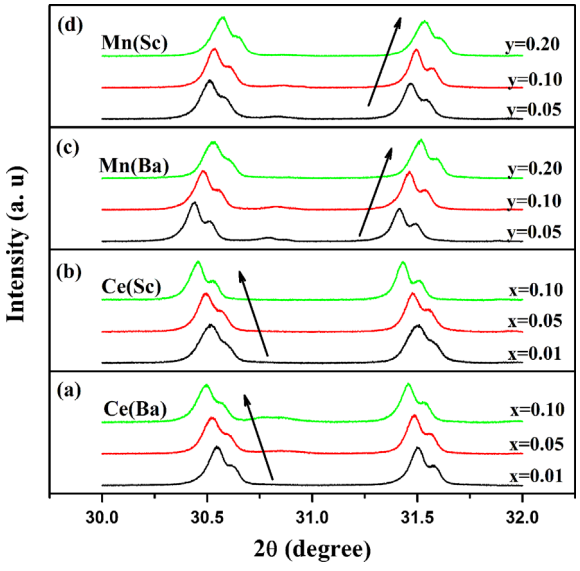

Fig. 1. XRD patterns of samples with the nominal compositions of (a) $(Ba_{9-x}Ce_x)Sc_2(SiO_4)_6$, (b) $Ba_9(Sc_{2-x}Ce_x)(SiO_4)_6$, (c) $(Ba_{9-y}Mn_y)Sc_2(SiO_4)_6$, and (d) $Ba_9(Sc_{2-y}Mn_y)(SiO_4)_6$ (x=0.01 − 0.10 and y=0.05 − 0.20).

On the basis of the effective ionic radii of cations with different CN reported by Shannon [12], the ionic radii of Ba^{2+} ions are 1.47, 1.52, and 1.61 Å with CN=9, 10, and 12, respectively. The ionic radius of Sc^{3+} is 0.745 Å with CN=6. For Ce^{3+}, the radii are 1.01, 1.196, 1.25, and 1.34 Å with CN=6, 9, 10, and 12, respectively. For Mn^{2+}, the radius is 0.83 Å with CN=6. In one word, both the ionic radius of Ce^{3+} and Mn^{2+} are smaller than that of Ba^{2+} but larger than that of Sc^{3+}. Accordingly, a lattice contraction takes place when Ce^{3+} or Mn^{2+} substitutes for Ba^{2+} but a lattice expansion takes place when Ce^{3+} or Mn^{2+} substitutes for Sc^{3+}. Therefore, the lattice expansions observed in the replacements of Ce^{3+} either for Ba^{2+} or for Sc^{3+} denote the preferable location of Ce^{3+} at the Sc^{3+} sites, while the lattice contractions in the replacements of Mn^{2+} either for Ba^{2+} or for Sc^{3+} denote the preferable location of Mn^{2+} at the Ba^{2+} sites.

Fig. 2 presents the XRD profiles of $Ba_9(Sc_{1.95}Ce_{0.05})(SiO_4)_6$ (BSS:0.05Ce^{3+}), $(Ba_{8.8}Mn_{0.2})Sc_2(SiO_4)_6$ (BSS:0.2Mn^{2+}), and $(Ba_{8.8}Mn_{0.2})(Sc_{1.95}Ce_{0.05})(SiO_4)_6$ (BSS:0.05Ce^{3+}, 0.2Mn^{2+}). No detectable impurity phase is observed even at high doping concentration of Ce^{3+} and Mn^{2+}, that is to say, all the samples remain to be the single phase of the BSS (PDF no. 82-1119).

3.2. Photoluminescence and ETs

Fig. 3 displays the optical properties of Ce^{3+} and Mn^{2+} in the BSS host materials. BSS:0.05Ce^{3+} exhibits an intense UV emission band peaked at 383 nm (Fig. 3(b)). The band can be decomposed into two Gaussian profiles peaked at 375 nm (26,670 cm^{-1}) and 404 nm (24,750 cm^{-1}) with energy difference of 1920 cm^{-1} (dash lines in Fig. 3(b)). This band is attributed to transitions from the lowest 5d energy level of Ce^{3+} to the $^2F_{5/2}$ and $^2F_{7/2}$ levels, respectively. The PLE spectrum of BSS:0.05Ce^{3+} shows two peaks at 328 and 247 nm. The asymmetric PLE band at 328 nm is ascribed to the Ce^{3+} 4f→5d transitions, consisting with the DR spectra of BSS:Ce^{3+} in Fig. 3(a). The other band at 247 nm may come from the absorption of the BSS host matrix or it may also be related to the high d-band of Ce^{3+}.

BSS:0.2Mn^{2+} exhibits a broad PL band peaked at 615 nm (Fig. 3 (c)), which can be assigned to the $^4T_1(4G)\rightarrow{}^6A_1(6S)$ transitions of Mn^{2+}. The corresponding PLE spectrum shows typical d–d transitions of Mn^{2+}. The transition is forbidden and difficult to be pumped, therefore, the emission is weak. It is noted that the Ce^{3+} emission overlaps with the Mn^{2+} excitation. Thus ETs from Ce^{3+} to Mn^{2+} are expected.

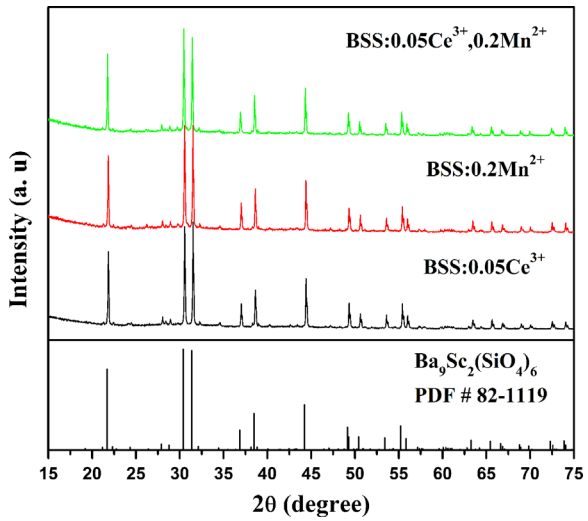

Fig. 2. XRD patterns of BSS:0.05Ce^{3+}, BSS:0.2Mn^{2+} and BSS:0.05Ce^{3+}, 0.2Mn^{2+}.

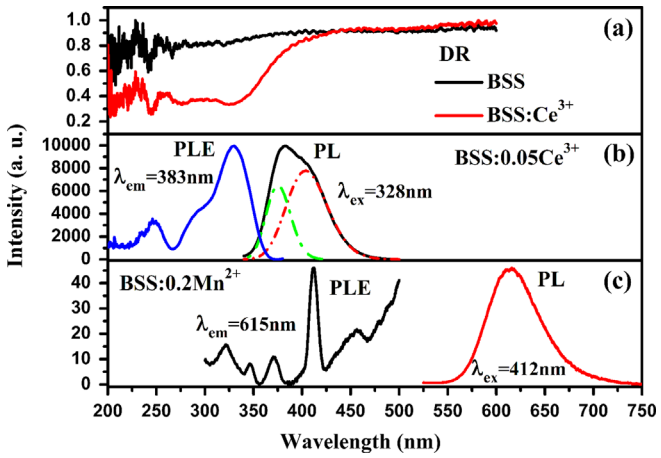

Fig. 3. DR spectra of BSS and BSS:0.05Ce^{3+} (a) and PL and PLE spectra of BSS:Ce^{3+} (b) and BSS:0.2Mn^{2+} (c).

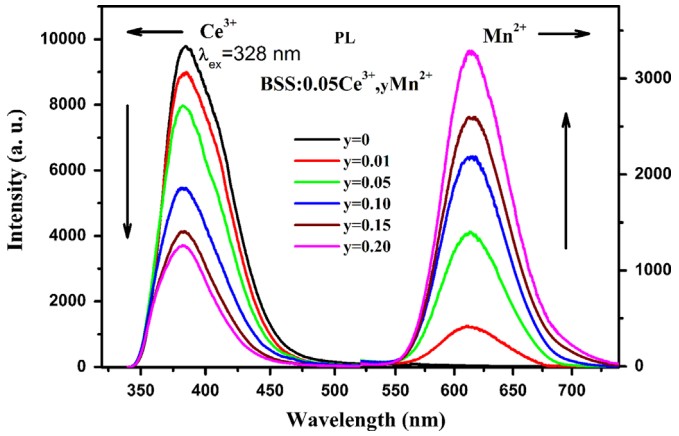

Fig. 4. PL spectra of Ce^{3+} and Mn^{2+} in BSS:0.05Ce^{3+}, $y$$Mn^{2+}$ (y=0−0.20) upon 328 nm excitation.

To study the $Ce^{3+}\rightarrow Mn^{2+}$ ETs, the PL spectra for samples of BSS:0.05Ce^{3+}, $y$$Mn^{2+}$ (y=0.01–0.2) were measured. As Fig. 4 shows, the PL spectrum upon Ce^{3+} excitation at 328 nm exhibits not only the Ce^{3+} emission at 383 nm but also the Mn^{2+} emission at 615 nm. It is evident that the Mn^{2+} emissions in presence of Ce^{3+} are enhanced over two orders of magnitude than that in the Mn^{2+} singly doped BSS. With increasing Mn^{2+} concentration (y), the Ce^{3+} emissions decrease while the Mn^{2+} emissions increase and reach the strongest emission intensity at y=0.2, which indicates an effective $Ce^{3+}\rightarrow Mn^{2+}$ ETs.

The Ce^{3+} decay curves of BSS:0.05Ce^{3+}, $y$$Mn^{2+}$ monitored at 383 nm by using pulsed excitation at 328 nm can also give a strong evidence for the $Ce^{3+}\rightarrow Mn^{2+}$ ETs. In principle, the $Ce^{3+}\rightarrow Mn^{2+}$ ETs can shorten the lifetime of Ce^{3+}. As Fig. 5 shows, with increasing y the decay becomes faster following the variation from exponential to non-exponential pattern, which indicates the typical effect of the $Ce^{3+}\rightarrow Mn^{2+}$ ETs.

When ET rate between a donor and an acceptor is proportional to an inverse power of the distance r, α/r^{m}, then based on the Inokuti–Hirayama (I–H) model [13], the formula

$$I_D(t)=I_{D0}(t)f(t)=I_{D0}(t)\exp\left[-\frac{4}{3}\pi\Gamma\left(1-\frac{3}{m}\right)n_A\alpha^{3/m}t^{3/m}\right] \quad (1)$$

can be used to describe the depopulation of Ce^{3+} in the presence of the Mn^{2+}. In the formula, $I_{D0}(t)$ is the decay function of donors in the absence of acceptors, the function $f(t)$ characterizes the loss of excited Ce^{3+} due to one way ETs to the Mn^{2+}, α is a

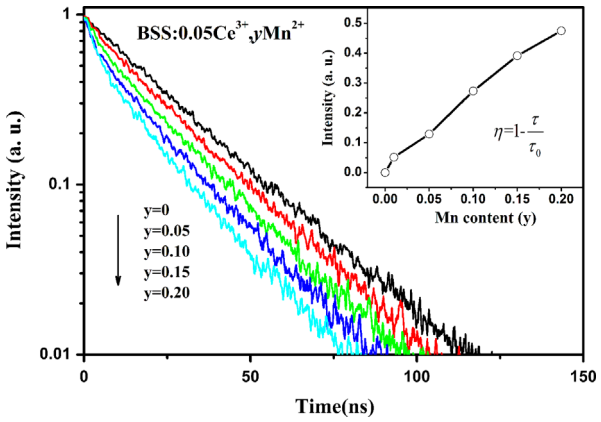

Fig. 5. Fluorescence lifetimes of series of BSS:0.05Ce^{3+}, $y$$Mn^{2+}$ (y=0−0.2) as a function of Mn^{2+} concentration. The inset shows the ET efficiency dependence on Mn^{2+} concentration.

microparameter for ETs, n_A is the number of acceptor ions per unit volume, and the interaction parameter m=6, 8, 10 for dipole–dipole, dipole–quadrupole, and quadrupole–quadrupole interaction, respectively. From Eq. (1), log{ln[1/$f(t)$]} acts as a linear function of log(t) with a slope of 3/m, and ln[$f(t)$] is proportional to $t^{3/m}$ with a slope of $-4\pi\Gamma(1-3/m)n_A\alpha^{3/m}/3$. The log–log plot of ln [1/$f(t)$] vs. t for sample y=0.2 is shown in Fig. 6(a). It is demonstrated that the slop for $t>10$ ns is 0.57, which indicating that m should be regarded as 6 and the interaction mechanism for the ETs is based on the dipole–dipole interaction. Fig. 6(b) shows the ln[$f(t)$] vs. $t^{1/2}$ for the samples of BSS:0.05Ce^{3+}, $y$$Mn^{2+}$ with y=0.1 and 0.2. The constant α taken as 8.4×10^{-37} $cm^6\,s^{-1}$ can be best fitting to each of the two curves. Considering there are 9 Ba^{2+} ions in the BSS host, the fractional concentration of Mn^{2+} is y/9. n_A is calculated by yN_{Ba}/9 with $N_{Ba}=1.458\times10^{22}$ cm^{-3} being the number of Ba^{2+} sites per unit volume in the BSS. The critical distance r_0 for the ETs can be calculated by the following equation [14]

$$\frac{\alpha}{r_0^6}=\frac{1}{\tau_0} \quad (2)$$

where τ_0 is the intrinsic lifetime of Ce^{3+} emission in the BSS that is 23.7 ns observed in BSS:0.05Ce^{3+}, which exhibits a pure exponential decay. Using Eq. (2), r_0 is calculated to be about 0.52 nm. In Fig. 6 (a) there is an increase of slope below 10 ns, forming a crossover [15]. The reason for this deviation is that Eq. (1) is not applicable for the time less than 10 ns in the present sample, since the equation is based on the assumption that the nearest distance between a donor and an acceptor to be 0, leading to an infinite initial ET rate.

Both fluorescence lifetimes of Ce^{3+} (τ) and Mn^{2+} (τ_1) for BSS:0.05Ce^{3+}, $y$$Mn^{2+}$ with y=0–0.2 are measured and represented in Table 1. The values of the lifetimes are obtained by integrating the decay curves of which the initial intensities are normalized. The lifetime of Mn^{2+} (τ_1) remains nearly constant, indicating Mn^{2+} concentration quenching not happened within the range of Mn^{2+} contents interested in this work. Based on the data represented in the Table 1, the ET efficiency η can be calculated by using

$$\eta=1-\frac{\tau}{\tau_0} \quad (3)$$

where τ is the lifetime of the donor in the presence of acceptor. The result is illustrated in the inset of Fig. 5. With increasing y, the ET efficiency increases gradually up to 48%.

Furthermore, the ET rate W between Ce^{3+} and Mn^{2+} can be expressed as $W=1/\tau-1/\tau_0$ [9]. Due to the unchanged fluorescence lifetimes of the Mn^{2+} ions listed in Table 1, the emission intensity ratio of the red Mn^{2+} emissions (named R) to the blue Ce^{3+}

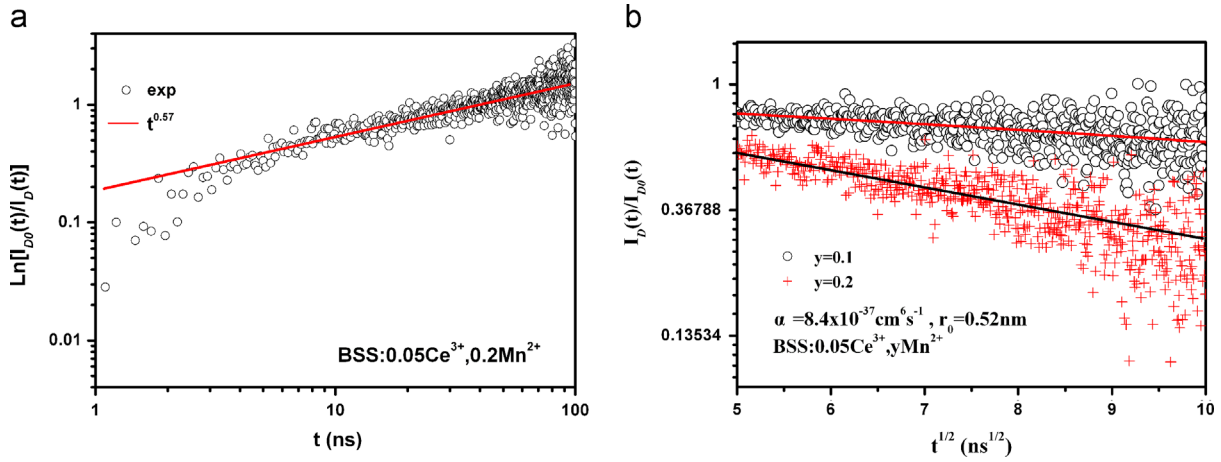

Fig. 6. Log–log plot of $\ln[1/f(t)]$ vs. t for sample BSS:0.05Ce^{3+}, 0.2Mn^{2+} (a) and plotted $\ln[f(t)]$ vs. $t^{1/2}$ for the samples BSS:0.05Ce^{3+}, $y$$Mn^{2+}$ (y=0.1 and 0.2) (b) the solid lines indicate the fitting behaviors.

Table 1
Fluorescent Lifetimes for Ce^{3+} (τ), Mn^{2+} (τ_1) in BSS:0.05Ce^{3+}, $y$$Mn^{2+}$

y	τ (ns)	τ_1 (ms)
0	23.7	/
0.01	22.4	17.1
0.05	20.6	17.4
0.10	17.2	17.5
0.15	14.4	17.5
0.20	12.4	17.3

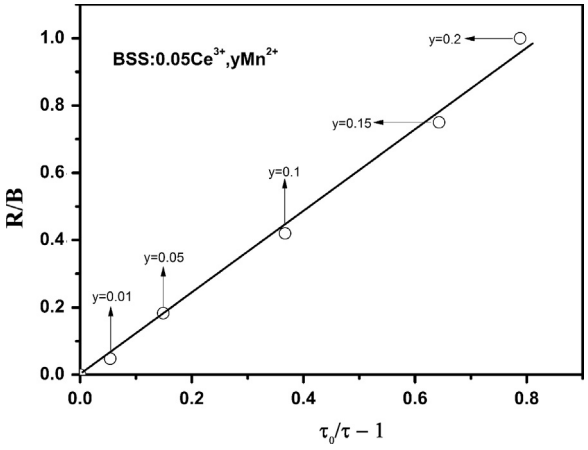

Fig. 7. The proportional relationship between R/B and $\tau_0/\tau-1$.

emissions (named B) can be expressed as $R/B=W\tau_0$, which is equal to $\tau_0/\tau-1$. As shown in Fig. 7, we plot R/B vs. $\tau_0/\tau-1$ for the sample series of BSS:0.05Ce^{3+}, $y$$Mn^{2+}$ with $y=0-0.2$. These experimental data exhibit a good proportional relationship where the R/B is normalized to the sample for y=0.2. This result indicates that the R/B ratio can be governed by the ET dynamics upon the UV excitation.

4. Conclusions

In summary, a novel BSS:Ce^{3+} phosphor exhibits an intense UV-blue emission in the range of 350–450 nm. Meanwhile, Mn^{2+} shows an intense red emission band peaked at 615 nm in BSS:Ce^{3+}, Mn^{2+} due to the effective $Ce^{3+}\rightarrow Mn^{2+}$ ETs. Non-radiative ETs from Ce^{3+} to Mn^{2+} in the BSS is governed by an electric dipole–dipole interaction. For Ce^{3+} concentration of 0.05, the corresponding rate constant and the critical distance are evaluated to be 8.4×10^{-37} cm^6 s^{-1} and 0.52 nm, respectively. The ET efficiency can reach 48%. The color-tunable luminescence with enhanced R/B intensity ratios can be performed through ETs from the blue Ce^{3+} to the red Mn^{2+} when the blue Ce^{3+} is excited by UV light. These results indicate that BSS:Ce^{3+}, Mn^{2+} phosphor can also be used as the red light source in the UV based white LEDs.

Acknowledgements

This work is supported by the National Natural Science Foundation of China (10834006, 51172226, 61275055, 10904141, 10904140) and the National High Technology Research and Development Program of China (2010AA03A404).

References

[1] S. Nakamura, T. Mukai, M. Senoh, Appl. Phys. Lett. 64 (1994) 1687.
[2] E.F. Schubert, J.K. Kim, Science 308 (2005) 1274.
[3] Y.D. Huh, J.H. Shim, Y. Kim, Y.R. Do, J. Electrochem. Soc. 150 (2003) 57.
[4] D.T. Palumbo, J.J. Brown, J. Electrochem. Soc. 117 (1970) 1184.
[5] D.T. Palumbo, J.J. Brown, J. Electrochem. Soc. 118 (1971) 1159.
[6] C.J. Duan, A.C.A. Delsing, H.T. Hintzen, Chem. Mater. 21 (2009) 1010.
[7] W. Liu, C. Huang, C. Yeh, J. Tsai, Y. Chiu, Y. Yeh, R. Liu, Inorg. Chem. 51 (2012) 9636.
[8] X. Xu, Y. Wang, X. Yu, Y. Li, Y. Gong, J. Am. Ceram. Soc. 94 (2011) 160.
[9] Y. Liu, X. Zhang, Z. Hao, Y. Luo, X. Wang, L. Ma, J. Zhang, J. Lumin. 133 (2013) 21.
[10] T. Nakano, Y. Kawakami, K. Uematsu, T. Ishigaki, K. Toda, M. Sato, J. Lumin. 129 (2009) 1654.
[11] L.H. Wang, L.F. Schneemeyer, R.J. Cava, T. Siegrist, J. Solid State Chem. 113 (1994) 211.
[12] R.D. Shannon, Acta Crystallogr. A32 (1976) 751.
[13] M. Inokuti, F. Hirayama, J. Chem. Phys. 43 (1965) 1978.
[14] L. Wang, X. Zhang, Z. Hao, Y. Luo, J. Zhang, X. Wang, J. Appl. Phys. 108 (2010) 093515.
[15] P.M. Selzer, D.L. Huber, B.B. Barnett, W.M. Yen, Phys. Rev. B: Condens. Matter 17 (1978) 4979.